Ion Velocity Measurements in the Magnetically Shielded Miniature (MaSMi) Hall Thruster Using Laser-Induced Fluorescence

IEPC-2019-531

Presented at the 36th International Electric Propulsion Conference
University of Vienna, Austria
September 15-20, 2019

Vernon H. Chaplin,* Ryan W. Conversano,† Alejandro Lopez Ortega,‡ Ioannis G. Mikellides,§
Robert B. Lobbia,¶ and Richard R. Hofer‖
Jet Propulsion Laboratory, California Institute of Technology, Pasadena, CA 91109, USA

We present laser-induced fluorescence (LIF) measurements of spatially resolved ion velocities in the Development Model Magnetically Shielded Miniature (MaSMi-DM) Hall Thruster, a high-performance low-power thruster operating at discharge powers from 150–1000 W. Mean axial velocity profiles along the channel centerline are presented at ten operating conditions spanning the throttle table, indicating that the acceleration region is located mostly outside the discharge channel, but further upstream than in some other magnetically shielded Hall thrusters. Integrating the steady state Vlasov equation in the upstream direction, starting with the measured axial ion velocity distribution function (IVDF) at a location approximately two channel lengths from the anode, shows that the broader IVDFs in the acceleration region are consistent with collisionless flow through the measured potential gradient, once spatial averaging over the $\sim$ 1 mm diameter measurement volume is accounted for. Therefore, the data allow us to rule out significant motion of the acceleration region during breathing mode oscillations, since this would act to further broaden the measured time-averaged IVDFs. Two-dimensional mean velocity vector maps in the vicinity of the acceleration region are shown for five operating conditions of particular interest for life assessment—the observed beam divergence is greater at low discharge power (200 W) than at high power (800–1000 W).

*Technologist, Electric Propulsion Group, vernon.h.chaplin@jpl.nasa.gov
†Technologist, Electric Propulsion Group, ryan.w.conversano@jpl.nasa.gov
‡Member of the Technical Staff, Electric Propulsion Group, alejandro.lopez.ortega@jpl.nasa.gov
§Principal Engineer, Electric Propulsion Group, ioannis.g.mikellides@jpl.nasa.gov
¶Technologist, Electric Propulsion Group, robert.b.lobbia@jpl.nasa.gov
‖Group Supervisor, Electric Propulsion Group, richard.r.hofer@jpl.nasa.gov

Nomenclature

JPL	= Jet Propulsion Laboratory
MaSMi	= Magnetically Shielded Miniature Hall Thruster
ASTRAEUS	= Ascendant Sub-kW Transcelestial Electric Propulsion System
MS	= Magnetically shielded
EM	= Engineering Model
DM	= Development Model
LIF	= Laser-induced fluorescence
IVDF	= Ion velocity distribution function
2D	= Two-dimensional
LaB_6	= Lanthanum hexaboride
DC	= Direct current (i.e., the time-averaged component of a signal)
AC	= Alternating current (i.e., the oscillatory component of a signal)
Xe II	= Singly ionized xenon
AOM	= Acousto-optic modulator
PMT	= Photomultiplier tube
z, r	= Axial, radial position coordinates
L	= Discharge channel length
V_d	= Discharge voltage
I_d	= Discharge current
v_z, v_r	= Axial, radial ion velocitiies
$f(v)$	= Ion velocity distribution function
v_{low}, v_{high}	= Lower, upper velocity limits for integration
ϕ	= Plasma potential
m_i	= Ion mass
e	= Electron charge
t	= Time
z_0, v_{z0}	= Reference position, and axial ion velocity at the reference position
$f_{meas}(z, v_z)$	= Measured axial IVDF with spatial averaging
$f_{local}(z, v_z)$	= Actual local IVDF without spatial averaging
Δz	= Half of the axial distance over which LIF data is spatially averaged
$G(z')$	= Gaussian spatial averaging function
σ	= Gaussian standard deviation
HERMeS	= Hall Effect Rocket with Magnetic Shielding

I. Introduction

NASA Jet Propulsion Laboratory (JPL) is developing the Magnetically Shielded Miniature (MaSMi) Hall Thruster[1] as part of the Ascendant Sub-kW Transcelestial Electric Propulsion System (ASTRAEUS),[2] which is designed to have the performance and lifetime necessary to enable small satellites to visit bodies of scientific interest throughout the Solar System. MaSMi has demonstrated best-in-class efficiency over a wide throttling range spanning discharge powers from 150–1000 W and discharge voltages from 200–500 V. Details on the thruster design and previous testing are presented in Refs.[1–6]

Magnetically shielded (MS) thrusters[7–10] have negligible discharge channel erosion, so thruster service life is ultimately expected to be limited by other wear mechanisms such as erosion of the front poles or cathode keeper. To inform design choices for the MaSMi Engineering Model (EM) thruster, lifetime analysis at several throttle points was carried out using the Hall2De code,[11,12] validated in part through short duration wear tests on a MaSMi Development Model (DM) thruster.[13] These multi-fluid simulations require experimental measurements of the acceleration zone location in order to determine the plasma potential profile, which is affected by non-classical electron transport across the radial magnetic field.[14–18] The necessary data can be obtained using laser-induced fluorescence (LIF),[19,20] a powerful technique for non-invasively measuring the spatial dependence of the ion velocity distribution function (IVDF) in a plasma. Once the IVDF is known as a function of position, the electric field that accelerated the ions can be calculated analytically[21] or inferred through comparisons with simulations.[22]

Voltage	Current	Power
200 V	0.75 A	150 W
200 V	**1.0 A**	**200 W**
300 V	1.5 A	450 W
400 V	1.5 A	600 W
200 V	**4.0 A**	**800 W**
300 V	2.67 A	800 W
400 V	**2.0 A**	**800 W**
300 V	**3.33 A**	**1000 W**
400 V	2.5 A	1000 W
500 V	**2.0 A**	**1000 W**

Table 1. MaSMi operating conditions studied with LIF. Data at a series of closely spaced points along the channel centerline were acquired at all operating conditions, and 2D vector maps were also acquired at conditions listed in bold.

In this paper, we present time-averaged LIF measurements of ion velocity distribution functions (IVDFs), mean velocities, and plasma potentials in the channel and near plume of MaSMi. The operating conditions studied are listed in Table 1. At each condition, the magnetic field strength setting that optimized performance and stability was used. Mean velocity profiles along the channel centerline were used to set the anomalous transport profile in the Hall2De simulations.[11] 2D velocity vector maps spanning the full channel width were compared with the model results for more detailed validation of the predicted ion velocities.

Section II describes the experimental setup including the thruster, facility, and LIF system. LIF measurements of axial velocities along the channel centerline are presented in Sec. III. Trends in the acceleration region location and shape as a function of operating condition are discussed, and a kinetic analysis is presented demonstrating that there were no significant temporal oscillations in the position of the acceleration region. Sec. IV presents high-resolution velocity vector maps at the conditions highlighted in Table 1, and conclusions are presented in Sec. V.

II. Experimental Setup

A. Thruster and Facility

The experiments were carried out on the MaSMi-DM,[5,6] the fourth generation research model MaSMi thruster. Key design features in common with the engineering model MaSMi-EM currently in development for ASTRAEUS include a centrally mounted heaterless LaB_6 hollow cathode and an advanced anode manifold optimized for high ionization efficiency.[23] The magnet coil currents at each operating condition were slightly modified from the standard MaSMi-DM settings in order to reproduce the field topology expected to be produced by the lower-mass magnetic circuit in MaSMi-EM (as predicted by simulations using the commercial software MagNet 3D).

The tests were carried out in the JPL High Bay vacuum facility, a 2.6 meter diameter $\times$ 5.2 meter length cylindrical chamber with graphite-coated surfaces downstream of the thruster and pumping speed of $\sim$ 40 kL/s in the configuration used for this test. In addition to LIF, active telemetry during the test campaign included thermocouples internal to the thruster (backpole, inner coil, and front outer pole) and on the LIF stages and optical assemblies, along with DC and high-speed AC measurements of discharge voltage, discharge current, cathode-to-ground voltage, and cathode keeper voltage.

B. LIF Setup

The LIF setup used a 500 mW amplified tunable diode laser, split along multiple beam paths and fiber-coupled into the vacuum chamber, to probe the 834.953 nm (in vacuum) electron transition of singly-ionized xenon (Xe II), with fluorescence detected at 542.06 nm. At a given laser wavelength, the fluorescence signal was proportional to the local density of metastable ions with velocity along the beam direction such that the Doppler-shifted laser wavelength in the ion rest frame was sufficiently close to 834.953 nm. An "axial" injection optic was mounted 1 meter downstream of the thruster in the ion beam (shielded by a water-cooled graphite panel and borosilicate window) in order to directly measure the axial IVDF. Two additional "diagonal" injection optics were mounted at 45 degree angles to the thruster centerline (orthogonal to one another) in order to measure the velocity vector (see Ref. 22). The collection optic was mounted above the thruster, approximately 60 degrees out of the plane containing the injection beams (i.e., the thruster's vertical midplane).

The axial injection beam was π-polarized (i.e., the laser beam electric field was approximately aligned with the thruster's radial magnetic field) in order to minimize Zeeman splitting for an accurate measurement of the width of the axial IVDFs.[24] The diagonal injection beams could not be π-polarized, so they were left unpolarized. The beams were chopped with acousto-optic modulators (AOMs), and the fluorescence signal was fiber coupled to a photomultiplier tube (PMT) and then processed by lock-in amplifiers, enabling data to be taken along multiple lines of sight simultaneously.

The injection and collection lines of sight were focused and aligned to intersect at a single stationary point, and the thruster was translated on dual axis motion stages to probe different regions of the plasma. Prior to chamber pump-down, initial alignment was carried out with leveling tools, rulers, and low-power visible lasers to ensure that the following conditions were satisfied:

- Thruster and motion stages were level
- Motion stages were aligned perpendicular to one another
- Axial stage direction of motion was aligned along the bolt pattern on the chamber floor
- Thruster was rotated so that its face was parallel to the radial stage direction of motion
- Injection beams were level and vertically located at the thruster midplane
- Diagonal injection optics were aligned at 45 degree angles with respect to the thruster centerline
- Axial injection optic was aligned parallel to the thruster centerline
- All three injection optics and the collection optic were aligned and focused to intersect at a single location

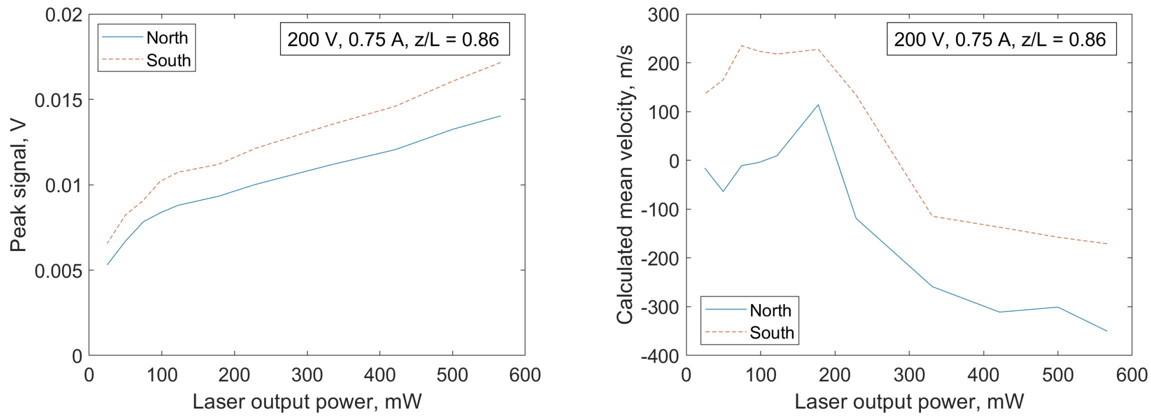

Figure 1. Saturation study data, varying the laser power while holding the measurement location and thruster operating condition constant. Left: LIF signal at the line peak. "North" and "South" refer to the two beam injection directions offset 45 degrees from axial and radial. Right: Calculated mean velocities from the first moment of the LIF data.

Achromatic lenses were used to achieve near-ideal focusing of the beams emitted from the multimode optical fibers. The diameter of the interrogation volume (corresponding to the spatial resolution of the measurement) was approximately 1 mm.

Each injection optic was mounted on remotely controlled dual-axis fine motion stages, allowing for alignment adjustments to compensate for thermal drift following pump-down and during thruster operation. Visible lasers were directed through the optics onto reference locations on the thruster face in order to determine the measurement volume location in the thruster coordinate system. The thruster stage motion was monitored with calibrated string pots in addition to the stepper motor indices. For additional details on the JPL LIF system and basic analysis techniques, refer to Refs. 22 and 25.

C. LIF Saturation Study

Saturation of the LIF signal occurs at relatively high laser intensities when the upper level population density of the targeted transition becomes comparable to the lower level population density and stimulated emission starts to compete with spontaneous emission. A typical threshold intensity for saturation[25,26] is ~ 0.1 mW/mm^2. It is well-known that saturation can lead to "power broadening" of the IVDF, artificially inflating the apparent ion temperature.[20,25] On the other hand, many authors have assumed that there is negligible effect on the mean velocity calculated from the LIF data. However, recent measurements at JPL prior to the MaSMi test campaign found as much as ~ 500 m/s shift in the apparent mean velocity as the laser power was increased to values in excess of 100 times the saturation intensity. The distortion appears to be caused by the various hyperfine structure components of Xe II saturating at different rates. Work is in progress to develop a procedure to deconvolve the saturated hyperfine line shape from the Doppler broadened profile.

Prior to commencing LIF data acquisition for MaSMi, a saturation study was carried out to identify the maximum permissible laser power before saturation began to significantly affect the mean velocity (apart from saturation considerations, it was desirable to operate with the laser intensity as high as possible for good signal-to-noise ratio). The data was taken at the 200 V, 0.75 A operating condition at a location on the channel centerline upstream of the acceleration region where the mean velocity was near 0. The saturation behavior should not depend explicitly on the operating condition, but it is possible that the mean velocity distortion could be dependent on the width of the Doppler profile at different locations in the plasma.

Results of the saturation study are shown in Fig. 1. Beams were injected along the two diagonal directions simultaneously, with two different chopper frequencies as described in Sec. II.B. The power values shown were measured near the laser on the optical table—the power coupled into the 1 mm diameter measurement spot was 6.6% of these values for the North diagonal injection optic, 12.5% for the South diagonal injection optic, and 4% for the Axial injection optic (the lower power for the North beam relative to the South beam was due to an unequal beam splitter, and the Axial beam was attenuated by the polarizer used in that optic).

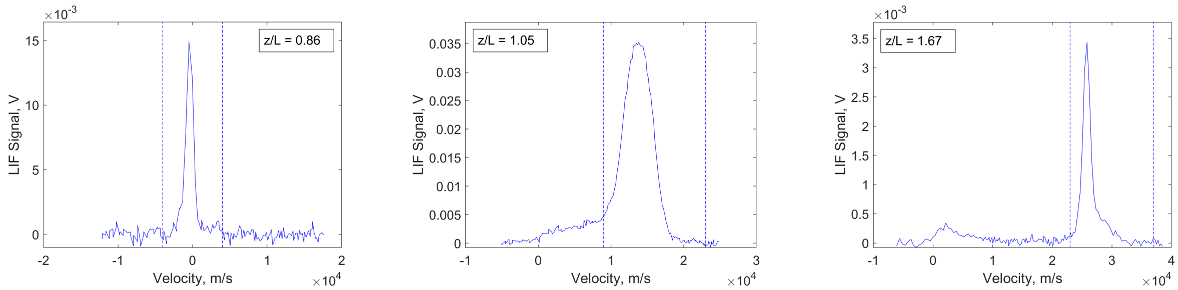

Figure 2. Measured IVDFs at the 500 V, 2 A operating condition in the ionization region (left), acceleration region (center), and near plume (right). Dashed lines show the integration range for the "fast population" first moment calculation.

Based on the results shown in the figure, $\sim$ 180 mW was selected as an appropriate laser amplifier setting for simultaneous measurements along the North and South diagonal axes. A power level $\sim$ 3 times higher was used axial measurements, since the power into the spot for Axial injection was $\sim$ 3 times lower than that for South injection. It is interesting to note that the threshold for avoiding mean velocity distortion was approximately the same for the South and North axes even though the South laser intensity was a factor of 2 higher, and the two signals should have been isolated from one another by lock-in amplification. It appears that the observed saturation behavior was caused by a combination of stimulated emission, as described above, and overall depletion of the metastable ion population by the two beams.[25]

III. Channel Centerline LIF Results

A. Mean Velocities and Potentials

Figure 2 shows examples of the raw IVDF data on the channel centerline at discharge voltage $V_d = 500$ V and discharge current $I_d = 2$ A. Throughout this paper, axial positions z are measured with respect to the anode and radial positions r are measured from the thruster centerline, and both are normalized to the channel length L. The mean velocity was calculated from the first moment of each IVDF, i.e.:

$$\langle v_z \rangle = \frac{\int_{v_{low}}^{v_{high}} v_z f(v_z)\, dv_z}{\int_{v_{low}}^{v_{high}} f(v_z)\, dv_z}, \tag{1}$$

where $f(v_z)$ is the measured IVDF. In order to determine the spatial dependence of the anomalous transport for the Hall2De simulations, it was desired to estimate the plasma potential from the velocity data. Therefore, the integration range was restricted to include only the main "fast" ion population born near the anode potential—the integration bounds v_{low} and v_{high} are shown with dashed lines on the IVDFs. The measured distributions in the acceleration region and downstream also contained a low-energy tail consisting of ions born from charge exchange and ionization at sub-anode potentials. The choice of a lower integration bound for the fast population velocity calculation is subjective, and there will be some error introduced by imprecise accounting for the true shape of this population's velocity distribution in the region where it overlaps with the slow population. However, this technique has proven to be a valuable tool for comparisons with simulations, giving smoother plots of velocity versus position than those obtained by considering only the most probable ion velocity. An alternate approach would be to fit a Gaussian function to the fast ion peak, but this is also an approximation because the fast population IVDF is not always Maxwellian.

Figure 3 shows the calculated fast population mean axial velocities for a selection of MaSMi operating conditions. The 200 V, 1 A dataset was extended further into the channel than the others in an attempt to resolve whether the velocity decreased monotonically moving toward the anode or reached a minimum, a distinction that was important for validating the neutral gas model and the impact of charge exchange in Hall2De. The measured velocity profile at $z/L < 0.75$ was flat to within the experimental uncertainty.

The error bars on the plots denote the 95% confidence interval for the mean velocity based on a bootstrap resampling[27,28] analysis of the random scatter in the raw data. Details on this method are provided in Ref. 29. The signal-to-noise ratios for these datasets were generally high, and the random uncertainties were small everywhere except deep in the channel. The accuracy specification of the self-calibrating wavelength

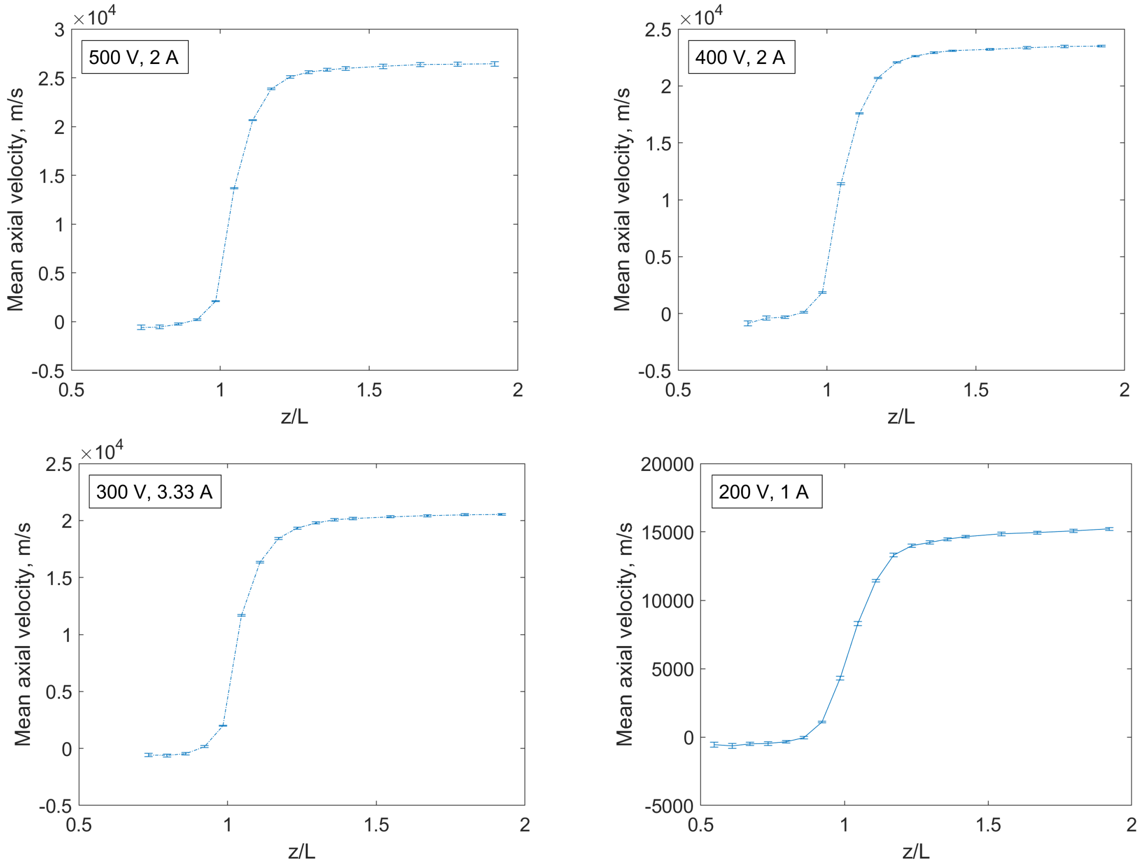

Figure 3. Fast population mean axial velocities along the channel centerline at four operating conditions.

meter (Toptica WS/7) adds ±50 m/s uncertainty in the velocity that is not accounted for in the error bars, and there is also up to ±180 m/s systematic uncertainty because the LIF transition wavelength was only known to three decimal places, and no stationary wavelength reference was used. Uncertainty in the position of the measurement volume was estimated to be ~ 0.5 mm, consistent with the high level of repeatability that was achieved in the location of the acceleration region measured at the same operating condition on different days.

The plasma potential profile at each operating condition was calculated by assuming that ions traveling at the mean velocity of the fast population were born at the anode potential,[22] so energy conservation gives

$$\phi(z) = V_d - \frac{m_i \langle v_z \rangle^2}{2e}. \tag{2}$$

The radial velocity component along the channel centerline was very small, as shown in Sec. IV, and was neglected. Results are shown in Fig. 4. At all operating conditions studied, the acceleration zone began just upstream of the channel exit. This position is upstream of its location in the 6 kW H6MS thruster[30] and in the 200 W ISCT200-MS thruster[31,32] and is similar to the time-averaged location in the 12.5 kW HERMeS thruster at $V_d = 400$–600 V.[22] The location of the peak electric field is near the radial magnetic field peak and is far enough upstream that pole erosion rates have been acceptable at all conditions modeled[11] and studied in wear tests.[13]

From Fig. 4 we note that the length of the acceleration region was similar at all conditions, with higher peak axial electrical field at higher V_d. At fixed V_d, the acceleration region was located slightly further upstream at higher I_d (with the exception of the 200 V, 4 A condition, which had a steeper plasma potential gradient than the low-current 200 V conditions) and the net ion accelerating voltage increased with I_d. The thruster exhibited excellent voltage utilization efficiency at its higher current operating conditions: for example, at the 400 V, 2.5 A condition, the kinetic energy of ions traveling at the fast population mean velocity at $z/L = 1.92$ was 386.5 eV.

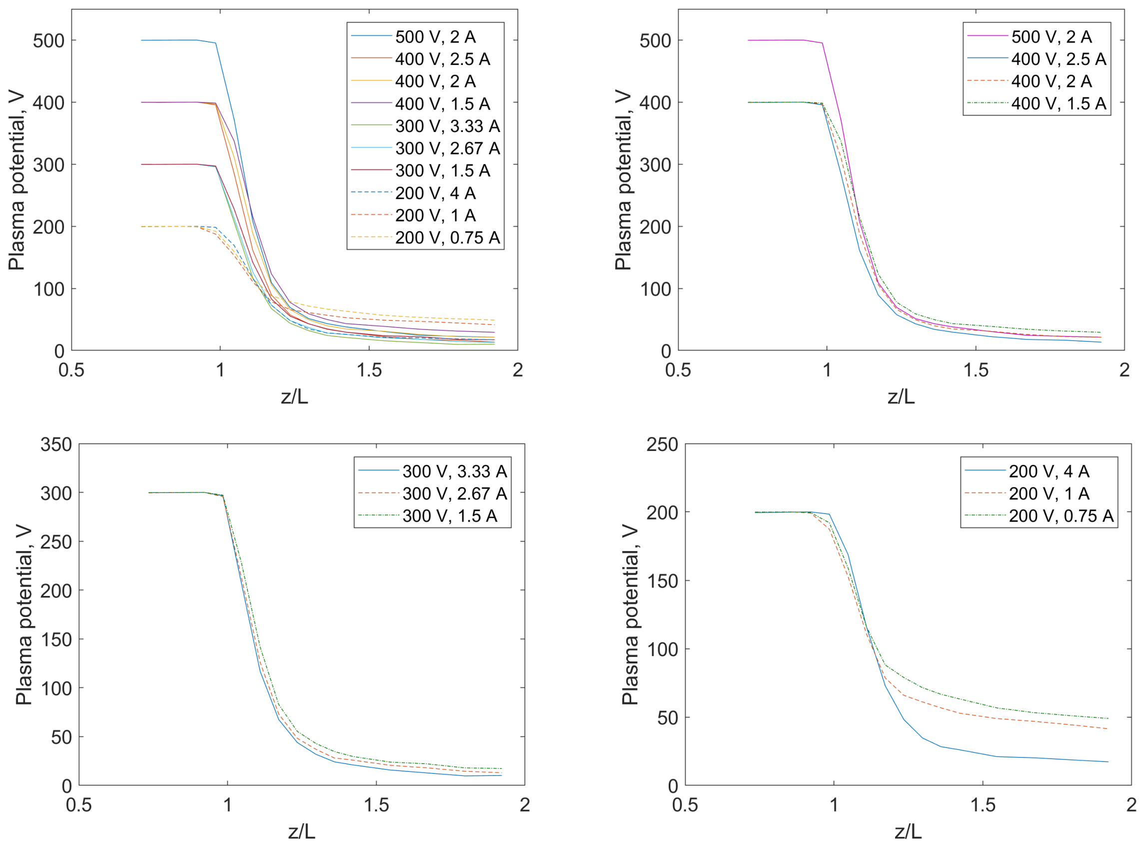

Figure 4. Plasma potential (referenced to cathode potential) along the channel centerline, estimated from the measured mean axial velocities. Upper left: All operating conditions. Upper right: 400–500 V conditions. Lower left: 300 V conditions. Lower right: 200 V conditions.

The voltage utilization efficiency was lowest at the 150–200 W operating conditions, and the IVDFs for these conditions revealed relatively large populations of low-velocity ions in the plume, suggesting that the neutral gas was not as efficiently ionized as it was at higher power. These trends are typical for Hall thrusters operating at very low power and are consistent with performance data.[6] The ability of MaSMi to throttle down from 1000 W all the way to 150 W is nevertheless a valuable feature for proposed NASA missions to destinations as far from the Sun as Neptune.[2]

B. Kinetic Analysis of IVDFs: Evidence Against Acceleration Zone Movement

At all operating conditions, the measured IVDFs were broadest in the acceleration region (see Fig. 2). One possible source of such broadening in time-averaged LIF data is temporal oscillations in the acceleration zone location, which have been observed in the HERMeS thruster[22,29] as well as unshielded Hall thrusters.[33,34] In HERMeS, the amplitude of these oscillations is large enough at high discharge voltages that the time-averaged IVDFs in the acceleration region have two peaks, and the oscillations have been found to increase the inner pole erosion rate by a factor of ~ 5.[35] Given the extent to which acceleration region movement could impact MaSMi's service life, it was important to use LIF to ensure that the Hall2De simulations were including an appropriate level of oscillations. It was possible to do this without taking time-resolved LIF measurements by calculating whether other known effects were sufficient to account for the broadening of the measured time-averaged IVDFs in the acceleration region without including any oscillations.

Downstream of the acceleration region, the ions are nearly collisionless and the ionization and charge exchange rates are low, so the axial IVDF evolution is approximately described by the 1D Vlasov equation:

$$0 = \frac{\partial f}{\partial t} + v_z \frac{\partial f}{\partial z} + a_z \frac{\partial f}{\partial v_z} = \frac{df}{dt}, \tag{3}$$

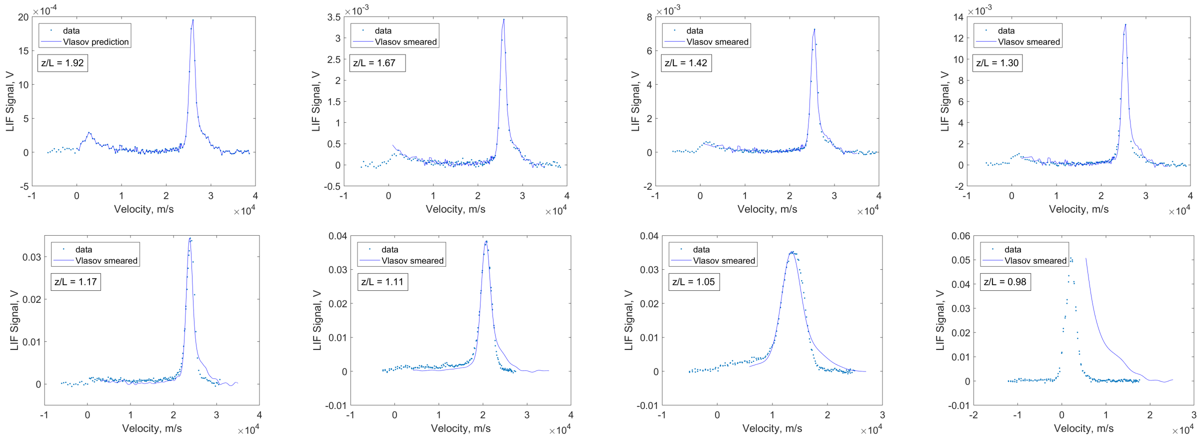

Figure 5. Measured channel centerline IVDFs (dots) at 500 V, 2 A compared with theoretical IVDFs (solid lines) calculated from the Vlasov equation using Eq. 5 with spatial averaging applied according to Eq. 6.

where a_z is the ion acceleration due to the axial electric field and df/dt is the total derivative of the IVDF, i.e., the derivative along an ion's trajectory through phase space. Since the IVDF is constant along a phase space trajectory, any function of a constant of the motion (such as energy) will be a solution of the Vlasov equation.[22,36] We can define a constant of the motion that is equal to the velocity at position $z = z_0$:

$$v_{z0} = \sqrt{\frac{2E}{m_i}} = \sqrt{v_z^2 + \frac{2e\left(\phi(z) - \phi(z_0)\right)}{m_i}}, \tag{4}$$

where E is the ion's total energy if we define the zero of potential to be at $z = z_0$. Given the IVDF $f(z_0, v_z)$ at this location, we can calculate the IVDF at other locations simply by transforming the velocity variable according to:

$$v_z \to \sqrt{v_{z0}^2 - \frac{2e\left(\phi(z) - \phi(z_0)\right)}{m_i}}. \tag{5}$$

Starting with the LIF data at the furthest downstream location probed ($z/L = 1.92$), the Vlasov equation was integrated in the upstream direction using Eq. 5 to see if the measured spatial dependence matched the expectation for simple collisionless evolution of the IVDF in the presence of an electric field. One aspect of this expectation was that the IVDF would be broader in the acceleration region than further downstream due to the well-known effect called "kinematic compression".[22,37] Integrating "backwards" (opposite the actual ion direction of motion) was preferred in order to avoid considering collisional regions of the plasma, and also because significant ion heating was detected in the acceleration region, as discussed below. For this analysis, the potential $\phi(z)$ was estimated using the most probable ion velocity in Eq. 2 rather than the fast population mean velocity, which included the high-energy tail visible in the right panel of Fig. 2.

Due to the steep velocity gradient in the acceleration zone (see Fig. 3), particularly at higher discharge voltages, the ~ 1 mm diameter measurement volume encompassed positions with a relatively wide range of mean ion velocities, and spatial averaging over this volume artificially broadened the measured IVDFs. This effect was simulated by assuming that the measurement volume had a Gaussian spatial profile and then adding up contributions to the LIF signal from different axial positions in this volume to get the measured IVDF with the smearing effect included:

$$f_{meas}(z, v_z) \propto \int_{z-\Delta z}^{z+\Delta z} G(z')\, f_{local}(z', v_z)\, dz', \tag{6}$$

where $\Delta z \equiv 1$ mm and

$$G(z') = \frac{1}{\sqrt{2\pi\sigma^2}} \exp\left(-\frac{(z'-z)^2}{2\sigma^2}\right), \tag{7}$$

with $\sigma \equiv 0.25$ mm so that 95% of the measured signal was assumed to originate from within 0.5 mm of the nominal measurement location z.

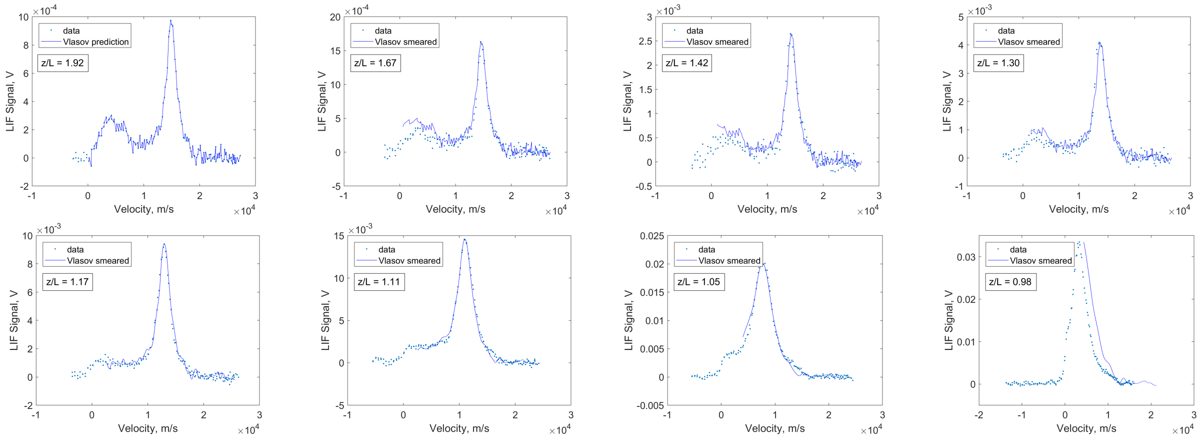

Figure 6. Same as Fig. 5, for the 200 V, 1 A operating condition.

The results of this calculation for the 500 V, 2 A operating condition are shown in Fig. 5. The magnitude of the predicted peak LIF signal at each location was rescaled to match the peak height in the data. The theory accurately predicts the width of the IVDF in the acceleration region ($z/L = 1.11$ and $z/L = 1.05$), implying that oscillations in the acceleration zone location did not contribute significantly to the observed IVDF broadening.

The theory also predicts that due to kinematic compression as the ions fell through the potential gradient, the IVDF would have had to be much wider than was measured at $z/L = 0.98$ in order for collisionless flow to produce the measured IVDFs further downstream. This implies that there must have been significant ion heating between $z/L = 0.98$ and $z/L = 1.05$. This axial IVDF broadening at the upstream edge of the acceleration region is also evident in LIF data from HERMeS[22] and the SPT-140,[38] as well as other Hall thrusters.[39] It has been attributed to overlap of the ionization and acceleration regions,[33,39] but kinetic analysis of HERMeS LIF data showed that there must be another important heating effect in this thruster, and the same conclusion appears to apply to MaSMi. The data at $z/L = 1.05$ feature a low-energy tail consisting of ions born at sub-anode potentials, but these ions were mostly born with velocities near 0 and thus they cannot fully explain the width of the main IVDF peak, which should have been kinematically compressed substantially by $z/L = 1.05$. Note that the theoretical IVDFs in Fig. 5 were cut off at low velocities (most noticeably at $z/L = 0.98$) in order to avoid the inconvenience of dealing with negative signs under the square root in Eq. 5 (which would require consideration of multiple cases to calculate the full IVDF).

The 200 V, 1 A operating condition was also treated with a Vlasov analysis because it had the highest discharge oscillation amplitude ($I_{d,p2p}/\langle I_d \rangle \approx 1.5$) among the conditions studied.[6] The results are shown in Fig. 6. Like at 500 V, 2 A, integrating backwards from $z/L = 1.92$ and including spatial averaging over the LIF measurement volume was sufficient to account for the measured width of the IVDFs in the acceleration region, without allowing for any oscillatory movement of the potential profile. A greater ion energy spread (effective axial temperature) existed in the near plume at $V_d = 200$ V compared to at $V_d = 500$ V because there was less kinematic compression with the smaller accelerating voltage.

In the 500 V, 2 A IVDFs (Fig. 5), it is interesting to notice the significant population of suprathermal ions in the near plume, a feature that is more or less absent in the 200 V, 1 A IVDFs (the small tail that does appear to exist on the high-energy side of these distributions may be caused by a hyperfine structure peak). The Vlasov theory begins to overpredict the number of suprathermal ions at $z/L \leq 1.42$, suggesting that this very high velocity population was mostly created between $z/L = 1.11$ and $z/L = 1.42$. Also note that the "backwards integrating" theory underpredicts the measured population of low-energy ions at $z/L = 1.11$ in Fig. 5, while we would have expected the opposite result given that new slow ion creation by charge exchange and ionization were neglected in the calculation. This may imply that the metastable ion population evolved somewhat differently for slow ions, and thus LIF using a metastable target state did not precisely reproduce the actual IVDF for all ions over this velocity range. Fortunately, the fast ion peak was of primary interest for applications to Hall2De modeling.

IV. Velocity Vector Maps

2D velocity vector maps were created from IVDFs measured along the two diagonal injection axes (see Sec. II). Figure 7 shows the vectors obtained by integrating over the entire IVDF using Eq. 1. Vector plots were also created with a limited first moment integration range isolating the fast ion population born near the anode potential, so that potential contours could be estimated and comparisons could be made with the velocity of the analogous main beam ion fluid in Hall2De.[40] Results are shown along with a selection of IVDFs in Figs. 8–12.

For these 2D data, it was necessary to assume without direct verification that the "fast ions" identified along one diagonal axis corresponded to the same ion population as the "fast ions" identified along the other axis. The analysis was relatively unambiguous close to the channel centerline, as in the center and bottom plots on the right-hand side of Fig. 8. Along the centerline, the mean fast population axial velocities calculated from a linear combination of the two diagonal velocity vectors were validated against the axial injection data presented in Sec. III.A, and very close agreement was obtained. On the other hand, at locations in the beam edges (e.g., the upper-right, lower-left, and center-left plots in Fig. 8), there were often peaks along one axis that fell on opposite sides of $v = 0$. In these cases the "fast ions" were assumed to be the population with the more positive velocity, because slower ions would more easily have their trajectories bent radially by the primarily radially-directed electric field at the beam edges just beyond the channel exit and thus could plausibly end up with a negative velocity along one diagonal axis. For cases in which two separate populations were not visible along one axis (e.g., the upper-left plot in Fig. 8), the integration bounds for that axis were set to encompass all ions. If a fast population could not be identified along either axis, the point was omitted from the fast population vector plot.

It is apparent from comparing Figs. 8 and 9 that the IVDFs were quite similar at the 500 V, 2 A and 400 V, 2 A operating conditions. The 500 V, 2 A fast population velocity vectors are overlaid with those for the 200 V, 1 A operating condition in the left panel of Fig. 13. The 200 V, 1 A vectors are significantly more radially divergent, despite nearly identical magnetic field topologies at the two conditions. The 200 V, 1 A velocity vectors were also more divergent than those measured at the 200 V, 4 A condition, as shown in the right panel of Fig. 13, helping to explain the lower efficiency at low discharge current.[6] High beam divergence was identified as a cause of sub-optimal performance in the previous iteration of the MaSMi thruster (MaSMi-60),[4] and the magnetic circuit was redesigned in MaSMi-DM in order to avoid an over-shielded magnetic field configuration.[5] This modification was partly responsible for the improved performance of MaSMi-DM,[5,6] and by pushing the radial magnetic field peak upstream it also had the beneficial side effect of moving the acceleration region upstream, thereby reducing the line of sight to the poles for high-energy ions at the beam edges.[11,30] However, the LIF results demonstrate that there are additional factors beyond magnetic field topology that can significantly affect beam divergence in the near plume.

V. Conclusion

We have presented results from a comprehensive study of ion velocity distributions as a function of position in MaSMi-DM, a high-performance magnetically shielded Hall thruster operating in the 150–1000 W discharge power range. Axial velocity profiles as well as 2D velocity vector maps obtained from measurements along diagonal lines of sight offset 45 degrees from axial/radial were presented. The acceleration region was located just beyond the channel exit at all operating conditions. A kinetic analysis of the axial data demonstrated that any oscillations in the plasma potential profile were too small to significantly broaden the measured time-averaged IVDFs in the acceleration region. The measured velocity vectors are being compared with Hall2De simulation results,[11] helping to provide confidence in the validity of these simulations for predicting the performance and pole erosion rates over the course of the thruster's life.

Acknowledgments

This research was carried out at the Jet Propulsion Laboratory, California Institute of Technology, under a contract with the National Aeronautics and Space Administration. The support of JPL's Research & Technology Development Strategic Initiative is gratefully acknowledged. The authors would also like to thank Ray Swindlehurst and Nowell Niblett for their assistance in maintaining the vacuum facility, and Kimberlyn Tilley for constructing the optical towers.

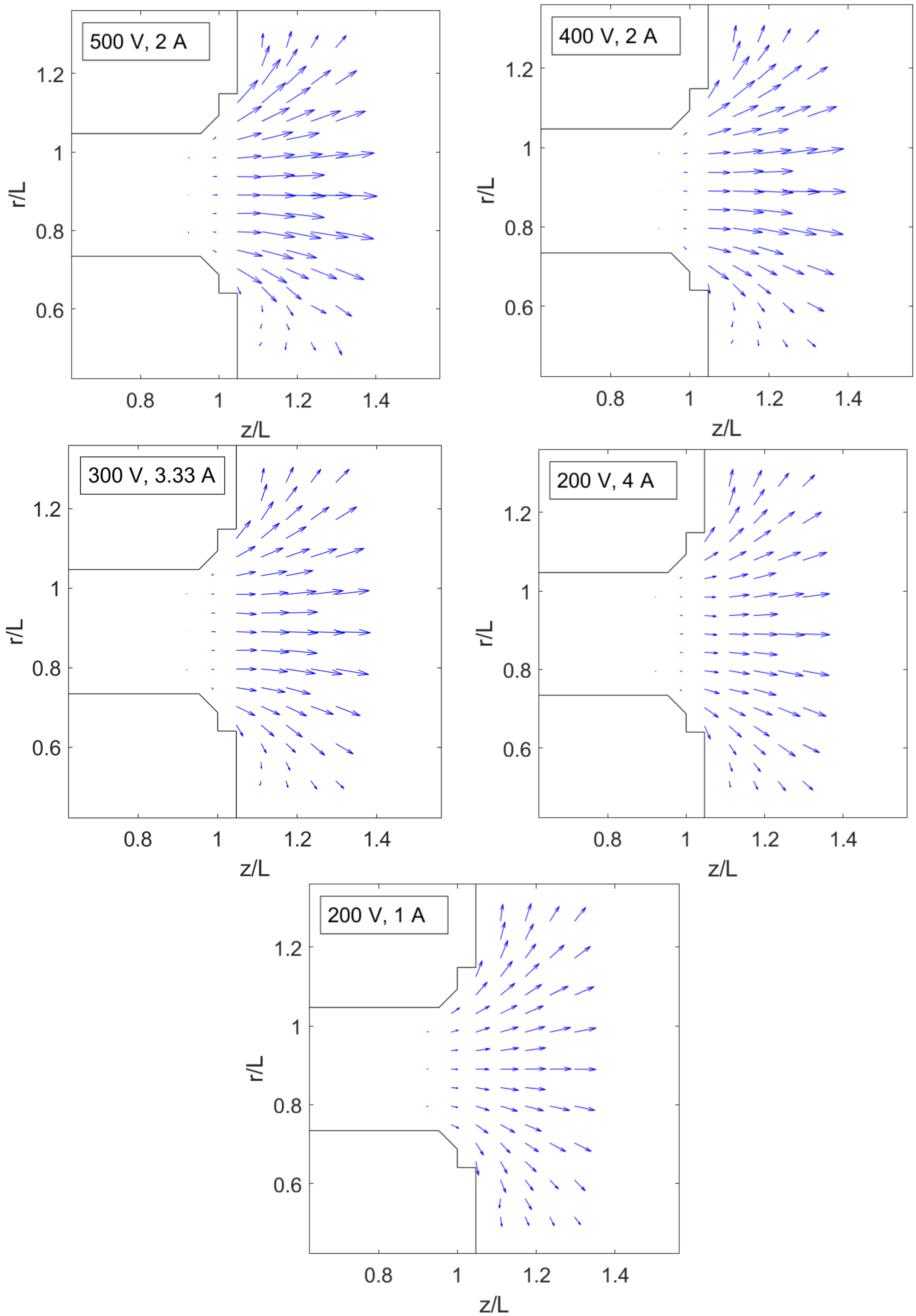

Figure 7. Mean velocity vectors for the full ion population at five MaSMi operating conditions.

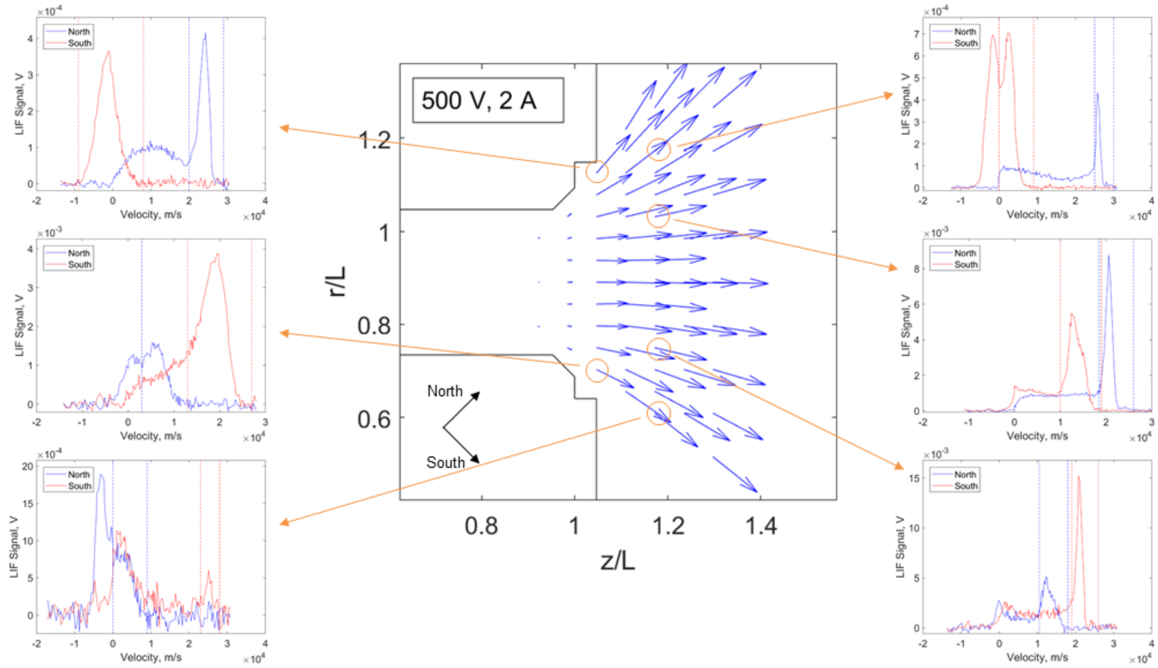

Figure 8. Examples of IVDFs at off-centerline locations, along with mean velocity vectors for the fast ion population, at the 500 V, 2 A operating condition. The integration bounds for the first moment calculation (Eq. 1) along each injection direction are denoted by dashed lines on the IVDF plots.

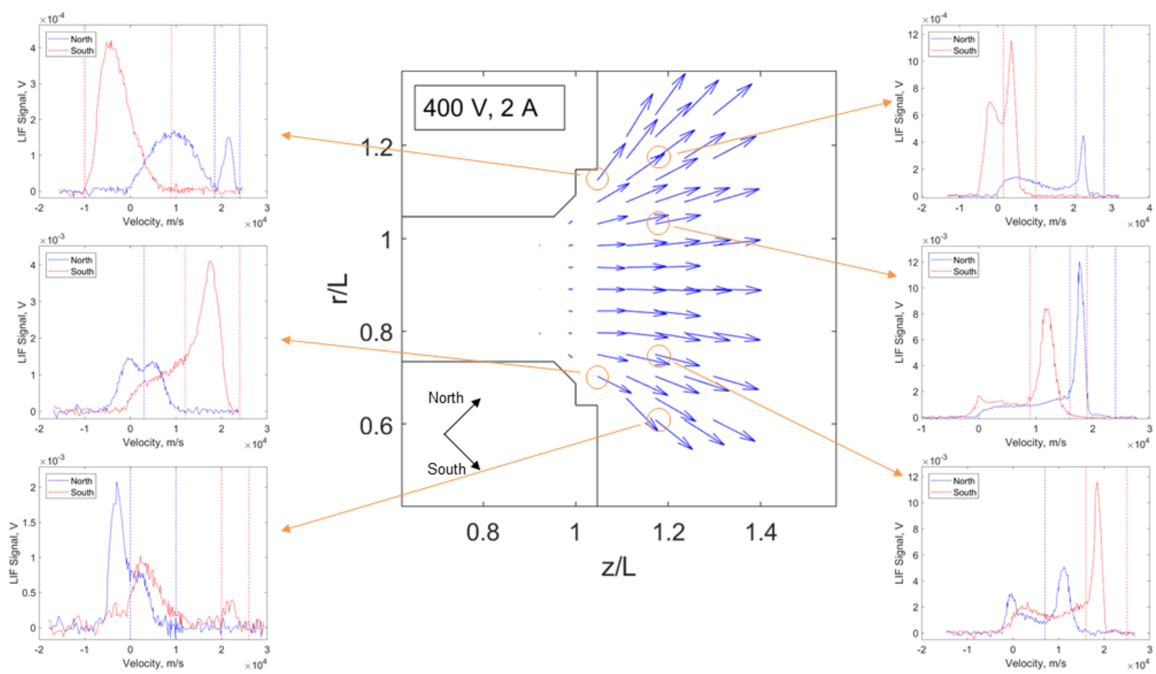

Figure 9. Same as Fig. 8, for the 400 V, 2 A operating condition.

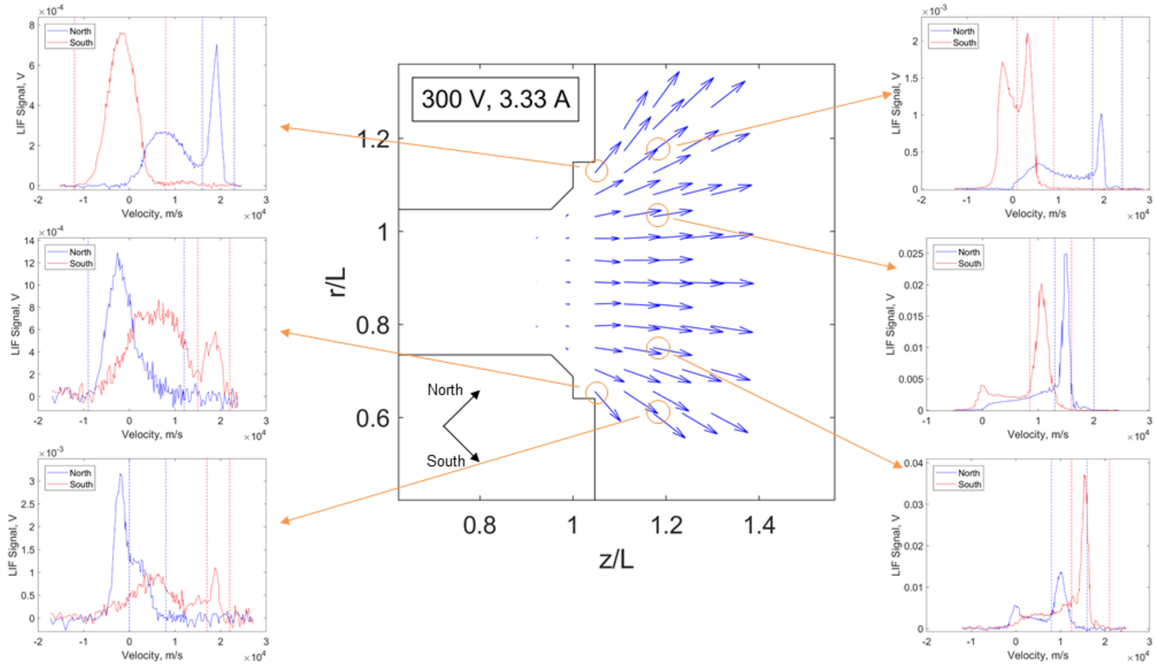

Figure 10. Same as Fig. 8, for the 300 V, 3.33 A operating condition.

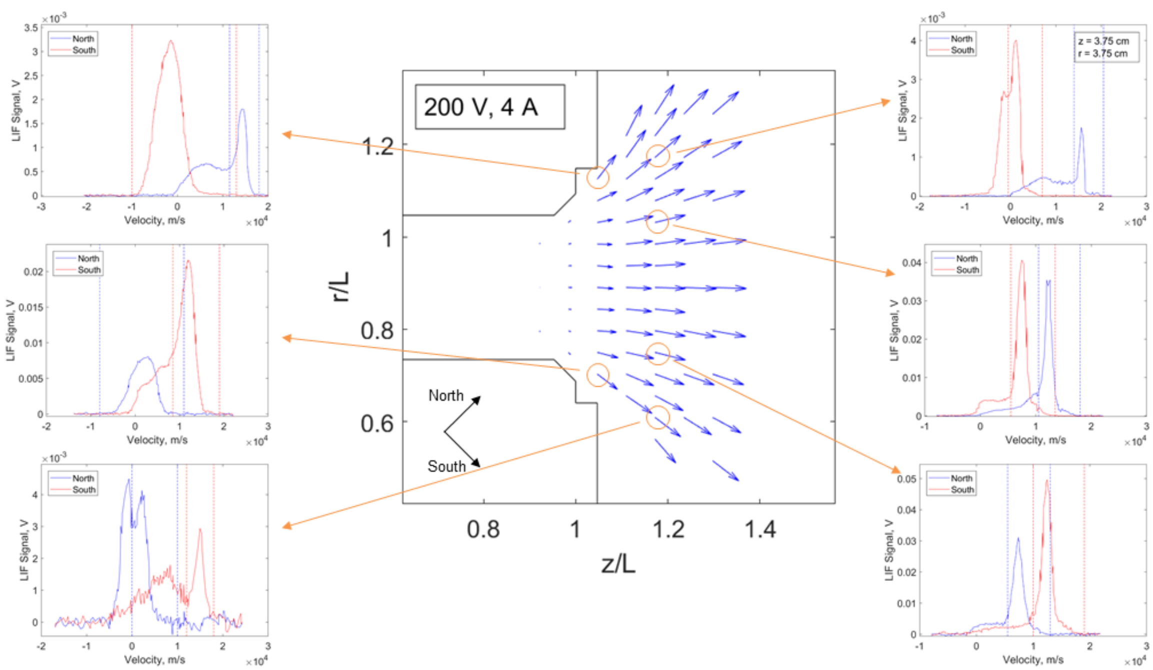

Figure 11. Same as Fig. 8, for the 200 V, 4 A operating condition.

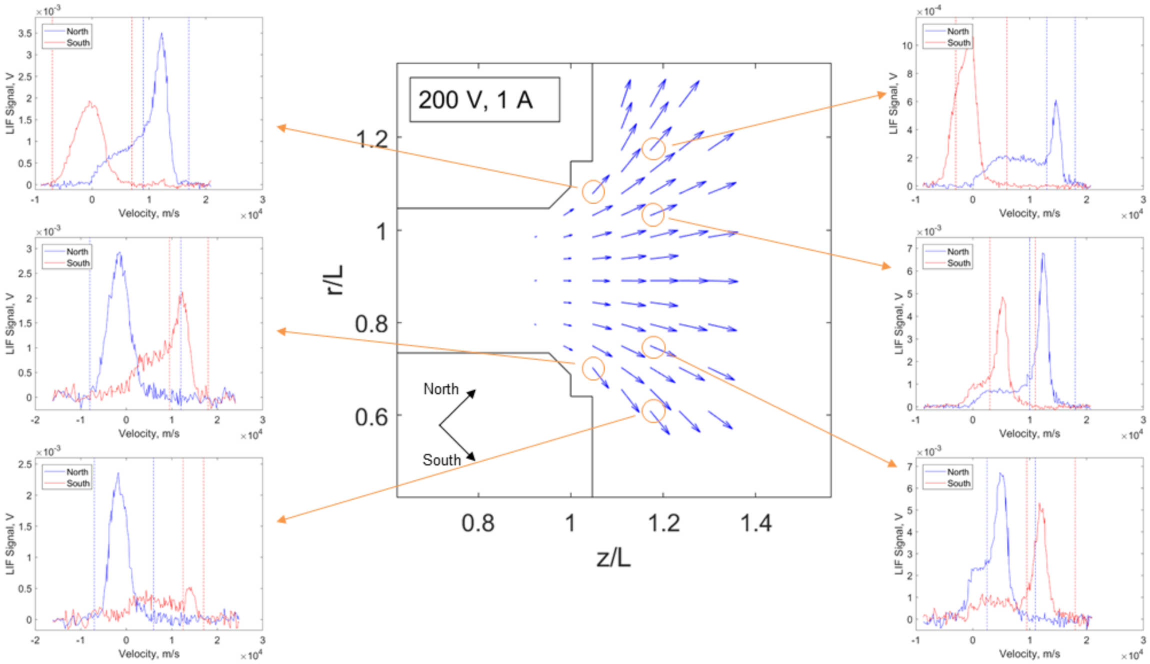

Figure 12. Same as Fig. 8, for the 200 V, 1 A operating condition.

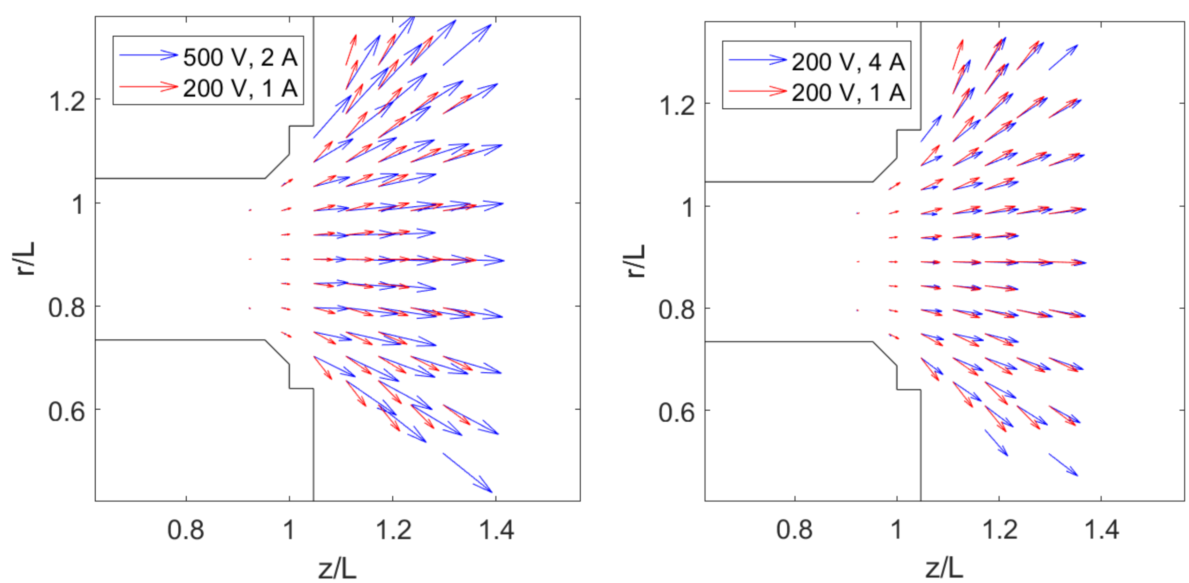

Figure 13. Comparisons of fast ion population velocity vectors for pairs of operating conditions. Left: 500 V, 2 A and 200 V, 1 A. Right: 200 V, 4 A and 200 V, 1 A.

References

[1] R. W. Conversano, S. W. Reilly, T. V. Kerber, J. W. Brooks, and D. M. Goebel. Development of and acceptance test preparations for the thruster component of the Ascendant Sub-kW Transcelestial Electric Propulsion System (ASTRAEUS). In *36th International Electric Propulsion Conference*, Vienna, Austria, September 2019. IEPC-2019-283.

[2] R. W. Conversano, A. Barchowsky, R. B. Lobbia, V. H. Chaplin, A. Lopez Ortega, J. A. Loveland, A. D. Lui, G. Becatti, S. W. Reilly, D. M. Goebel, J. S. Snyder, R. R. Hofer, T. M. Randolph, I. G. Mikellides, V. Vorperian, , G. A. Carr, J. Rapinchuk, C. Y. Villalpando, and D. Grebow. Overview of the Ascendant Sub-kW Transcelestial Electric Propulsion System. In *36th International Electric Propulsion Conference*, Vienna, Austria, September 2019. IEPC-2019-282.

[3] R. W. Conversano, D. M. Goebel, R. R. Hofer, I. G. Mikellides, and R. E. Wirz. Performance analysis of a low-power magnetically shielded Hall thruster: Experiments. *J. Propul. Power*, 33(4):975–983, 2017.

[4] R. W. Conversano, D. M. Goebel, I. G. Mikellides, R. R. Hofer, and R. E. Wirz. Performance analysis of a low-power magnetically shielded Hall thruster: Computational modeling. *J. Propul. Power*, 33(4):992–1001, 2017.

[5] R. W. Conversano, R. B. Lobbia, K. C. Tilley, D. M. Goebel, S. W. Reilly, I. G. Mikellides, and R. R. Hofer. Development and initial performance testing of a low-power magnetically shielded Hall thruster with an internally-mounted hollow cathode. In *35th International Electric Propulsion Conference*, Atlanta, GA, October 2017. IEPC-2017-64.

[6] R. W. Conversano, R. B. Lobbia, T. V. Kerber, K. C. Tilley, D. M. Goebel, S. W. Reilly, I. G. Mikellides, and R. R. Hofer. Performance characterization of a low-power magnetically shielded Hall thruster with an internally mounted hollow cathode. *Plasma Sources Sci. Technol.* Submitted for publication.

[7] I. G. Mikellides, I. Katz, R. R. Hofer, D. M. Goebel, K. de Grys, and A. Mathers. Magnetic shielding of the channel walls in a Hall plasma accelerator. *Phys. Plasmas*, 18:033501, 2011.

[8] R. R. Hofer, D. M. Goebel, I. G. Mikellides, and I. Katz. Magnetic shielding of a laboratory Hall thruster. II. Experiments. *J. Appl. Phys.*, 115:043304, 2014.

[9] I. G. Mikellides, I. Katz, R. R. Hofer, and D. M. Goebel. Magnetic shielding of a laboratory Hall thruster. I. Theory and validation. *J. Appl. Phys.*, 115:043303, 2014.

[10] R. Hofer, J. Polk, M. Sekerak, I. Mikellides, H. Kamhawi, T. Verhey, D. Herman, and G. Williams. The 12.5 kW Hall Effect Rocket with Magnetic Shielding (HERMeS) for the Asteroid Redirect Robotic Mission. In *52nd AIAA/SAE/ASEE Joint Propulsion Conference*, Salt Lake City, UT, July 2016. AIAA-2016-4825.

[11] A. Lopez Ortega, I. G. Mikellides, R. W. Conversano, R. B. Lobbia, and V. H. Chaplin. Plasma simulations for the assessment of pole erosion in the Magnetically Shielded Miniature Hall Thruster (MaSMi). In *36th International Electric Propulsion Conference*, Vienna, Austria, September 2019. IEPC-2019-281.

[12] I. G. Mikellides and I. Katz. Numerical simulations of Hall-effect plasma accelerators on a magnetic-field-aligned-mesh. *Phys. Rev. E*, 86:046703, 2012.

[13] R. B. Lobbia, et al. Pole erosion measurements for the development model of the Magnetically Shielded Miniature Hall Thruster (MaSMi-DM). In *36th International Electric Propulsion Conference*, Vienna, Austria, September 2019. IEPC-2019-298.

[14] N. B. Meezan, W. A. Hargus, and M. A. Cappelli. Anomalous electron mobility in a coaxial Hall discharge plasma. *Phys. Rev. E*, 63:026410, 2001.

[15] J. C. Adam, A. Héron, and G. Laval. Study of stationary plasma thrusters using two-dimensional fully kinetic simulations. *Phys. Plasmas*, 11:295, 2004.

[16] A. Lopez Ortega, I. Katz, and V. H. Chaplin. A first-principles model based on saturation of the electron cyclotron drift instability for electron transport in hydrodynamics simulations of Hall thruster plasmas. In *35th International Electric Propulsion Conference*, Atlanta, GA, October 2017. IEPC-2017-178.

[17] J. P. Boeuf and L. Garrigues. E $\times$ B electron drift instability in Hall thrusters: Particle-in-cell simulations vs. theory. *Phys. Plasmas*, 25:061204, 2018.

[18] S. Janhunen, A. Smolyakov, O. Chapurin, D. Sydorenko, I. Kaganovich, and Y. Raitses. Nonlinear structures and anomalous transport in partially magnetized E $\times$ B plasmas. *Phys. Plasmas*, 25:011608, 2018.

[19] R. A. Stern and J. A. Johnson, III. Plasma ion diagnostics using resonant fluorescence. *Phys. Rev. Lett.*, 34(25):1548–1551, 1975.

[20] R. J. Cedolin, Jr. W. A. Hargus, P. V. Storm, R. K. Hanson, and M. A. Cappelli. Laser-induced fluorescence study of a xenon Hall thruster. *Appl. Phys. B*, 65:459–469, 1997.

[21] J. Vaudolon and S. Mazouffre. Indirect determination of the electric field in plasma discharges using laser-induced fluorescence spectroscopy. *Phys. Plasmas*, 21:093505, 2014.

[22] V. H. Chaplin, B. A. Jorns, A. Lopez Ortega, I. G. Mikellides, R. W. Conversano, R. B. Lobbia, and R. R. Hofer. Laser-induced fluorescence measurements of acceleration zone scaling in the 12.5 kW HERMeS Hall thruster. *J. Appl. Phys.*, 124:183302, 2018.

[23] R. W. Conversano, D. M. Goebel, I. Katz, and R. R. Hofer. Low-power Hall thruster with an internally mounted low-current hollow cathode. US Patent No. 16/205,048, 2019.

[24] W. Huang. *Study of Hall Thruster Discharge Channel Wall Erosion via Optical Diagnostics*. PhD thesis, University of Michigan, 2011.

[25] V. H. Chaplin, B. A. Jorns, R. W. Conversano, R. B. Lobbia, A. Lopez Ortega, I .G. Mikellides, and R. R. Hofer. Laser-induced fluorescence measurements of the acceleration zone in the 12.5 kW HERMeS Hall thruster. In *35th International Electric Propulsion Conference*, Atlanta, GA, October 2017. IEPC-2017-229.

[26] G. Severn, D. Lee, and N. Herschkowitz. Xenon ion laser-induced fluorescence using a visible tunable diode laser near 680 nm. *Rev. Sci. Instrum.*, 78:116105, 2007.

[27] B. Efron. Bootstrap methods - another look at the jackknife. *Ann. Stat.*, 7(1):1–26, 1979.

[28]D. J. Gershman, J. C. Dorelli, A. F-Vinas, and C. J. Pollock. The calculation of moment uncertainties from velocity distribution functions with random errors. *J. Geophys. Res.-Space Phys.*, 120(8):6633–6645, 2015.

[29]V. H. Chaplin, R. B. Lobbia, A. Lopez Ortega, I. G. Mikellides, P. J. Roberts, A. J. Friss, J. S. Peter, R. R. Hofer, and J. E. Polk. Spatiotemporally resolved ion velocity distribution measurements in the 12.5 kW HERMeS Hall thruster. In *36th International Electric Propulsion Conference*, Vienna, Austria, September 2019. IEPC-2019-532.

[30]B. A. Jorns, C. Dodson, J. Anderson, D. M. Goebel, R. R. Hofer, M. Sekerak, A. Lopez Ortega, and I. G. Mikellides. Mechanisms for pole piece erosion in a 6-kW magnetically shielded Hall thruster. In *52nd AIAA/SAE/ASEE Joint Propulsion Conference*, Salt Lake City, UT, July 25–27 2016. AIAA-2016-4839.

[31]L. Grimaud and S. Mazouffre. Ion behavior in low-power magnetically shielded and unshielded Hall thrusters. *Plasma Sources Sci. Technol.*, 26:055020, 2017.

[32]L. Grimaud and S. Mazouffre. Conducting wall Hall thrusters in magnetic shielding and standard configurations. *J. Appl. Phys.*, 122:033305, 2017.

[33]S. Mazouffre, D. Gawron, and N. Sadeghi. A time-resolved laser induced fluorescence study on the ion velocity distribution function in a Hall thruster after a fast current disruption. *Phys. Plasmas*, 16:043504, 2009.

[34]A. L. Fabris, C. V. Young, and M. A. Cappelli. Time-resolved laser-induced fluorescence measurement of ion and neutral dynamics in a Hall thruster during ionization oscillations. *J. Appl. Phys.*, 118:233301, 2015.

[35]A. Lopez Ortega, I. Mikellides, and V. Chaplin. Hall2De simulations for the assessment of pole erosion in the 12.5 kW Hall Effect Rocket with Magnetic Shielding (HERMeS). In *35th International Electric Propulsion Conference*, Atlanta, GA, October 2017. IEPC-2017-154.

[36]P. M. Bellan. *Fundamentals of Plasma Physics*. Cambridge University Press, New York, 2006.

[37]T. B. Smith. *Deconvolution of Ion Velocity Distributions from Laser-Induced Fluorescence Spectra of Xenon Electrostatic Thruster Plumes*. PhD thesis, University of Michigan, 2003.

[38]J. S. Snyder, D. M. Goebel, V. H. Chaplin, A. Lopez Ortega, I. G. Mikellides, F. Aghazadeh, I. Johnson, T. Kerl, and G. Lenguito. Electric propulsion for the Psyche mission. In *36th International Electric Propulsion Conference*, Vienna, Austria, September 2019. IEPC-2019-244.

[39]S. Mazouffre. Laser-induced fluorescence diagnostics of the cross-field discharge of Hall thrusters. *Plasma Sources Sci. Technol.*, 22:013001, 2013.

[40]A. Lopez Ortega, I. G. Mikellides, M. J. Sekerak, and B. A. Jorns. Plasma simulations in 2-D (r-z) geometry for the assessment of pole erosion in a magnetically shielded Hall thruster. *J. Appl. Phys.*, 125:033302, 2019.